

**$v_2$  vs  $p_T$  and  $\eta$  in p+Au and  $^3He+Au$  200 GeV at RHIC**

by

**Theodore Koblesky**

B.S., University of Illinois, 2011

A thesis submitted to the  
Faculty of the Graduate School of the  
University of Colorado in partial fulfillment  
of the requirements for the degree of  
Doctor of Philosophy  
Department of Physics  
2016

This thesis entitled:  
 $v_2$  vs  $p_T$  and  $\eta$  in p+Au and  $^3He+Au$  200 GeV at RHIC  
written by Theodore Koblesky  
has been approved for the Department of Physics

---

Prof. James Nagle

---

Prof. Standin

---

Ms. Standin

Date \_\_\_\_\_

The final copy of this thesis has been examined by the signatories, and we find that both the content and the form meet acceptable presentation standards of scholarly work in the above mentioned discipline.

Koblesky, Theodore (Ph.D., High Energy Nuclear Physics)

$v_2$  vs  $p_T$  and  $\eta$  in p+Au and  $^3He+Au$  200 GeV at RHIC

Thesis directed by Prof. James Nagle

Abstract page

## **Dedication**

To some of the of the fluffy kitties.

## Acknowledgements

People

## Contents

### Chapter

<b>1</b>	<b>Introduction</b>	<b>2</b>
1.1	The Standard Model . . . . .	2
1.2	Quantum Chromodynamics . . . . .	2
1.3	Heavy Ion Collisions . . . . .	3
<b>2</b>	<b>Collectivity in QCD</b>	<b>5</b>
2.1	Conceptual Understanding of Flow . . . . .	5
2.2	Mathematical Introduction . . . . .	5
2.3	A Review of Flow Measurements in Heavy Ion Collisions . . . . .	6
2.4	Collectivity in Small QCD Systems . . . . .	6
2.4.1	Monte-Carlo Initial Condition Characterization . . . . .	6
<b>3</b>	<b>Experimental Setup</b>	<b>8</b>
3.1	RHIC . . . . .	8
3.2	PHENIX . . . . .	9
3.2.1	Event Categorization Detectors . . . . .	9
3.2.1.1	Beam Beam Counter (BBC) . . . . .	9
3.2.2	Forward Rapidity Detectors . . . . .	11
3.2.2.1	Forward Vertex Detector (FVTX) . . . . .	11
3.2.2.2	FVTX Clustering . . . . .	11

3.2.3	Midrapidity Detectors . . . . .	11
3.2.3.1	Drift Chamber . . . . .	11
3.2.3.2	Pad Chambers . . . . .	12
3.2.3.3	Ring Imaging Cherenkov Detector . . . . .	13
3.2.3.4	EM Cal . . . . .	13
3.2.3.5	Silicon Vertex Detector (SVX) . . . . .	13
3.2.4	DAQ . . . . .	13
3.2.4.1	Triggering . . . . .	14
3.3	Event Reconstruction and Characterization . . . . .	14
3.3.1	Central Arm Tracking . . . . .	14
3.3.2	CNT Tracks Simulation . . . . .	14
3.3.3	Centrality Determination . . . . .	14
3.3.4	Vertex Determination . . . . .	14
3.4	Run15 pAu Dataset . . . . .	14
3.4.1	Beam Geometry Effects . . . . .	14
<b>4</b>	<b>Analysis</b>	<b>17</b>
4.1	Direct Observables: Building Blocks of the Measurement . . . . .	17
4.1.1	Central Arm Tracks . . . . .	17
4.1.2	FVTX Clusters . . . . .	17
4.1.3	BBC PMTs . . . . .	18
4.2	Event Plane Method . . . . .	18
4.2.1	Event Plane Flattening Calibration . . . . .	20
4.2.2	Event Plane Resolution Calculation . . . . .	21
4.3	good run list . . . . .	22
4.4	luminosity over time . . . . .	22
4.5	bbc charge . . . . .	22

4.6	central events . . . . .	22
4.6.1	Correcting for Beam Geometry . . . . .	24
4.7	Systematic Error Estimate . . . . .	24
4.7.1	Non-flow Estimate . . . . .	24
4.7.2	Pile Up . . . . .	24
4.7.3	Beam Angle . . . . .	24
4.7.4	Track Background . . . . .	24
4.7.5	Event Plane Detectors Agreement . . . . .	24
<b>5</b>	<b>Discussion of Results</b>	<b>31</b>
5.1	$v_2$ Measurement . . . . .	31
5.1.1	$v_2$ vs $p_T$ . . . . .	31
5.1.2	$v_2$ vs Multiplicity . . . . .	31
5.2	Comparison with Theory . . . . .	31
5.2.1	SONIC . . . . .	31
5.2.2	AMPT . . . . .	31
5.2.3	IP-Glasma with Hydro . . . . .	31
5.3	Comparison with Other Species . . . . .	31
<b>6</b>	<b>Summary and Outlook</b>	<b>34</b>

## Appendix

## Tables

### Table

## Figures

### Figure

1.1	TBA	4
2.1	TBA	5
2.2	TBA	7
2.3	a) IP-glasma. b) MC-KLN. c) MC-Glauber.	7
3.1	TBA	9
3.2	TBA	11
3.3	FVTX/VTX cut	12
3.4	TBA	14
3.5	TBA	15
3.6	TBA	15
3.7	A vector diagram illustrating the yellow and blue beam angle.	15
3.8	On the left is a cartoon diagram illustrating $\eta$ acceptance shift due to a beam offset in one of the FVTXs layers. The right plot shows the AMPT distribution of particles for pAu @ 200 GeV and the shifted $\eta$ acceptance.	16

4.1	This is the FVTX-S $\Psi_2$ distribution projected over all z-vertex bins at different steps during the calibration. The range of the $\Psi_2$ resolution is from $-\frac{\pi}{2}$ to $\frac{\pi}{2}$ because of the periodicity. The raw (in red) $\Psi_2$ distribution has a sinusoidal shape. The re-centered (in green) $\Psi_2$ distribution moves the peak to 0.0 radians and changes the width. The flattened (in blue) $\Psi_2$ distribution spread out the counts so that there is uniformity. Each calibration step preserves the integral. . . . .	21
4.2	TBA . . . . .	23
4.3	BBC Psi2 EP distribution in different z vertex bins red before flattening, blue after flattening. . . . .	23
4.4	The left plot shows the FVTX EP East West Difference without any corrections and the right plot shows the BBC EP East West Difference without any corrections. . . . .	24
4.5	The left plot shows the FVTX EP East West Difference with beam rotation and vertex offset corrections and the right plot shows the BBC EP East West Difference with the same corrections. . . . .	24
4.6	TBA . . . . .	25
4.7	These figures show the phi distribution of BBC PMT charge in a) the Run15 pp dataset and in b) the Run15 pAu dataset. . . . .	25
4.8	TBA . . . . .	26
4.9	FVTX EP corrected with inverse $\phi$ weighting and 20 % cut. . . . .	26
4.10	TBA . . . . .	27
4.11	BBC EP corrected with pp, pau ratio weighting. . . . .	27
4.12	A comparison of FVTX EP $v_2$ corrections on the inclusive measurement. . . . .	28
4.13	TBA . . . . .	28
4.14	TBA . . . . .	29
4.15	TBA . . . . .	29
4.16	The left plot is an example of a normal event, the right plot is an example pile up event. . . . .	30

5.1	TBA	32
5.2	TBA	32
5.3	TBA	33

## **Contents**

# **Chapter 1**

## **Introduction**

### **1.1 The Standard Model**

The SM (Standard Model of particle physics) is humanity's best understanding of how the fundamental building blocks reality behave. The SM as we know it today has evolved over many years, beginning with the unification of the electromagnetic and weak forces in the late 1960's. The current evolution of the SM includes four fundamental forces, listed in Table (TBA), and 17 fundamental particles, listed in Table (TBA). Calculations using the SM have been remarkably successful at making precise predictions which have been confirmed experimentally. It is one of the most rigorously tested theories in physics and has held up remarkably well to years of experimental testing.

### **1.2 Quantum Chromodynamics**

In order to calculate things within the SM, we must turn to quantum field theory (QFT) to formally, mathematically describe the fundamental interactions in the SM. In order to calculate particles interacting via the strong force, the most relevant force at the high energies provided by hadron-hadron collisions at RHIC, we turn to QCD. Quantum chromodynamics introduces an additional quantum number to the SM and is governed by the SU(3) symmetry group. This new quantum number, labeled color, can take three values referred to as red (r), green (g), and blue (b), in an analogy to the three colors in optics. Like the electric charge in QED, each color has an opposite, ?negative? value, carried by the antiquarks, referred to as anti-red (r), anti-green (g),

and anti-blue(b).

### 1.3 Heavy Ion Collisions

The idea of hot hadronic matter was developed in the early 1950s by various physicists including Enrico Fermi [?]. This concept of applying statistical and hydrodynamical models to a strongly interacting particle ensemble ultimately evolved into the theory of QGP (Quark Gluon Plasma). Since then, systematic studies of hot hadronic matter systems have produced a greater understanding of the state of matter hypothesized to be QGP. QGP has been roughly mapped out in the hadronic phase diagram. The state of matter created in our laboratories is understood to be comparable to the universe about one microsecond after the big bang. And the evolution of the medium has been mapped from the initial heavy ion collision all the way to the final state particles.

Here is the timeline overview of heavy ion collisions in general: At the moment when heavy ions collide relativistically ( $\tau=0$ ), they are length contracted down to flat disks in the lab frame as seen in Figure .... Then, the initial geometry resulting from the shape of the collision overlap region and fluctuations within the nuclei is transformed into the initial energy density of the medium ( $\tau \sim 1 \text{ fm}/c$ ). At that moment, the hot hadronic matter is thought to be made up of deconfined quarks and gluons in thermal equilibrium, otherwise known as QGP. The system then evolves hydrodynamically, expanding along the pressure gradients present in the initial energy density. At a certain point during this expansion, the medium has cooled down enough in order to form baryons and mesons out of the quark gluon soup in a process known as hadronization. It is important to note that the medium is still in thermal equilibrium at this point but it is no longer known as QGP but instead as hadron gas. Once the medium has cooled down and expanded sufficiently, kinetic freeze-out occurs and the hadron gas becomes a group of particles which have ceased self-interaction ( $\tau \sim 10 \text{ fm}/c$ ). It is this group of final state particles which can be detected much later ( $\tau \sim 10^{15} \text{ fm}/c$ ). Although detectable particles escape the medium at all times, the vast majority of particles we detect are produced at kinetic freeze-out.

Although the field of high-energy nuclear physics is still evolving, several measured properties

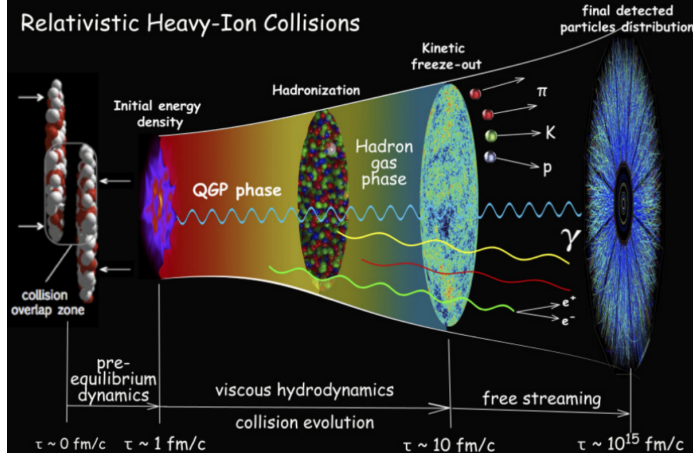


Figure 1.1: TBA

of this state of matter have come together to make QGP the prevailing explanation. Among the best observations indicating QGP are jet quenching,  $J/\psi$  melting, and elliptic flow. The observation of jets measured at much lower energies than expected imply that the jets are experiencing energy loss when interacting with a strongly coupled medium. The observation of a severe reduction in the number of expected  $J/\psi$  particles matches a prediction that a strongly coupled medium with a temperature above the Hagedorn temperature will melt  $J/\psi$  particles. Finally, an elliptic symmetry in the angular distribution of final state particles when viewed along the beam line has been observed. The translation of initial geometry into long-range angular correlations indicates collectivity in a strongly coupled medium.

## Chapter 2

### Collectivity in QCD

#### 2.1 Conceptual Understanding of Flow

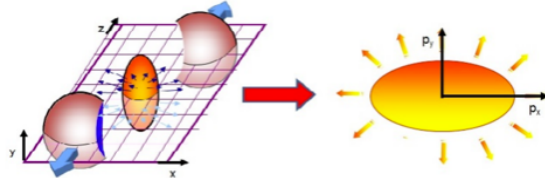


Figure 2.1: TBA

#### 2.2 Mathematical Introduction

A measurement of the azimuthal anisotropy is a way to quantify the extent of long-range angular correlation present in the medium evolution. One way to study the azimuthal anisotropy is to create a correlation function. The 2-particle correlation function method uses pairs of particles from the event in order to create a correlation function. For each pair in an event, a  $\Delta\phi$  value is obtained which makes up the signal  $S(\Delta\phi, p_T)$ . In order to correct for artificial correlations which would distort the distribution from detector effects or other sources, a mixed event background distribution  $M(\Delta\phi, p_T)$  is created. The correlation function can be defined as follows:

$$S(\Delta\phi, p_T) = \frac{d(w_{\text{PMT}} N_{\text{Same event}}^{\text{track}(p_T) - \text{PMT}})}{d\Delta\phi}, \quad (2.1)$$

$$C(\Delta\phi, p_T) = \frac{S(\Delta\phi, p_T)}{M(\Delta\phi, p_T)} \frac{\int_0^{2\pi} M(\Delta\phi, p_T) d\Delta\phi}{\int_0^{2\pi} S(\Delta\phi, p_T) d\Delta\phi}. \quad (2.2)$$

Substantial variations in this  $C(\Delta\phi, p_T)$  are usually seen as long-range angular correlations which can be attributed to collectivity.

In order to quantify the azimuthal anisotropy,  $C(\Delta\phi, p_T)$  is Fourier transformed:

$$C(\Delta\phi, p_T) \propto 1 + \sum_{n=1} 2v_n \cos(n[\phi(p_T) - \Psi_n]) \quad (2.3)$$

where  $\Psi_n$  is the event plane angle,  $\phi$  is the azimuth of tracks from the event, and  $v_n$  are flow coefficients. The measured  $v_n$  averaged over a single event is defined as:

$$v_n = \frac{\langle \cos(n[\phi - \Psi_n]) \rangle}{Res(\Psi_n)} \quad (2.4)$$

where  $Res(\Psi_n)$  is the event plane resolution for each event.  $v_N$  are further averaged over each event.

$$\varepsilon_n = \frac{\sqrt{\langle r^2 \cos(n\phi) \rangle^2 + \langle r^2 \sin(n\phi) \rangle^2}}{\langle r^2 \rangle} \quad (2.5)$$

### 2.3 A Review of Flow Measurements in Heavy Ion Collisions

### 2.4 Collectivity in Small QCD Systems

Small collision systems have been considered too small to create hot and dense matter. These systems were thought to be control experiments which could be used to measure cold nuclear matter effects. However, evidence of collectivity has recently been observed at RHIC in p+Au collisions at  $\sqrt{s_{NN}} = 200$  GeV in the most central collisions [?]. Although, the  $p_T$  dependent  $v_N$  has been measured, what has not been measured in these small systems is the degree to which  $v_N$  changes a function of rapidity. This is a particularly interesting measurement to make in an asymmetric collision system such as p+Au.

#### 2.4.1 Monte-Carlo Initial Condition Characterization

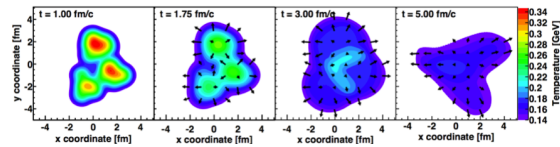


Figure 2.2: TBA

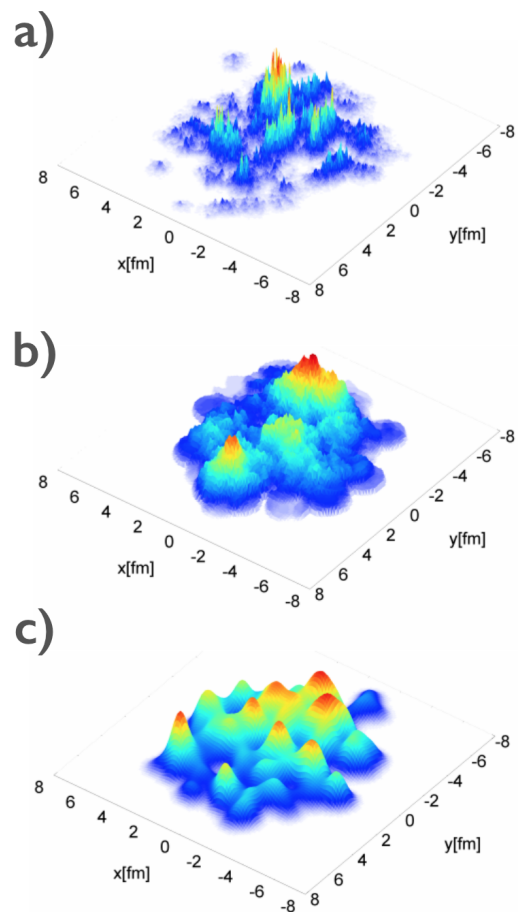


Figure 2.3: a) IP-glasma. b) MC-KLN. c) MC-Glauber.

## **Chapter 3**

### **Experimental Setup**

#### **3.1 RHIC**

The Relativistic Heavy Ion Collider (RHIC) is a superconducting charged hadron collider located at Brookhaven Nation Labs (BNL) in Upton, NY. RHIC is capable of accelerating heavy ions such as Au (gold) or Cu (copper) nuclei to energies of 200 GeV per nucleon. RHIC is also capable of accelerating lighter ions such as protons, deuteron, and helium to 200 GeV per nucleon and 510 GeV per nucleon in the case of protons. There are currently 2 major detector experiments operating in interaction regions around the RHIC ring: PHENIX and STAR. RHIC typically is operating for 5.5 months every year in what is called a "Run". A chain of smaller accelerators is used to "feed" the ions into RHIC, where they are accelerated (or decelerated in some circumstances) to the desired collision energy. For heavy ions such as Au, the process is listed below. . When the ions exit the Tandem Van De Graaff, . Then the Booster Synchrotron to 95 MeV per nucleon

- (1) A pulsed sputter Au ion source to generates negative ions in the Tandem Van De graaff.
- (2) The ions are passed through an electron stripping foil to achieve a positive 12 charge and accelerated to 1 MeV per nucleon.
- (3) The ions pass through magnets to further strip electrons and filter charge, yielding to a positive 32 charge state.
- (4) The ions are sent to the Booster Synchrotron which accelerates them to 95 MeV per nucleon and leaves them at a positive 77 charge.

- (5) The ions enter the Alternating Gradient Synchrotron (AGS) in 24-ion bunches. The ions are debunched and rebunched into 4 bunches and then accelerated to 10.8 GeV per nucleon.
- (6) The bunches then exit the AGS one at a time, where their Au ions are stripped of their 2 remaining electrons, yielding a final charge state of positive 79. Finally, the bunches are transferred to their respective buckets in RHIC.

There has been 16 "Runs" so far but the relevant run for this thesis was Run 15 taken in 2015 which was p+Au collisions at 200 GeV per nucleon.

### 3.2 PHENIX

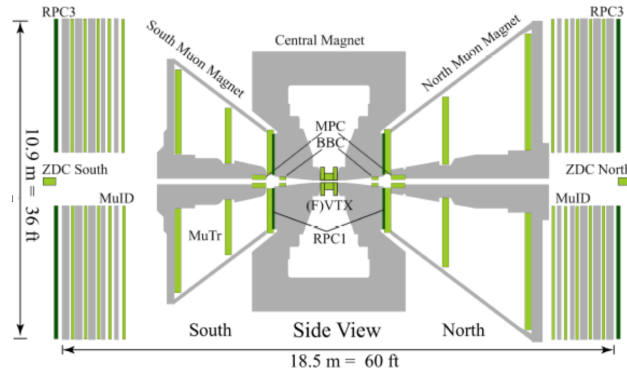


Figure 3.1: TBA

#### 3.2.1 Event Categorization Detectors

Talk about all detectors in this category including ZDC briefly.

##### 3.2.1.1 Beam Beam Counter (BBC)

The Beam Beam Counter (BBC) is a multipurpose detector used to determine the event start time, vertex, centrality, and is also one of several detectors capable of measuring ?EP . The BBC is composed of two mirror image arrays, a South and a North Arm, that surround the beam pipe 144 cm on opposite sides of the nominal collision point just behind the Central Magnet, covering

$3.0 \leq \eta \leq 3.9$  and  $2\pi$  radians in azimuth. Each BBC arm is made of 64 elements each composed of a 3-cm length quartz Cherenkov radiator connected to a 1-in diameter Hamamatsu R6178 mesh dynode PMT (photomultiplier tube), as shown in Fig (TBA). The outer and inner diameters of the BBC are 30 cm and 10 cm, respectively, allowing for a 1 cm clearance of the beam pipe. With a timing resolution of 524 ps, the BBC is used to mark the event start time for the entire PHENIX detector by averaging the emitted particles arrival time at each BBC arm. The timing difference between each arm is used to determine the collision's z-vertex or simply vertex or z by

$$z = c \frac{T_S - T_N}{2}, \quad (3.1)$$

where  $T_S, T_N$  are the particle's arrival times for each arm and  $c$  is the speed of light. In 200-GeV Au+Au collisions the BBC vertex resolution is 0.5 cm and the (x,y) collision position is always assumed to be (0,0). Determining the z-vertex aids in particle track reconstruction and in eliminating events that occurred outside the PHENIX acceptance of  $30 \text{ cm} < z < 30 \text{ cm}$ . The BBC is also used as a Level-1 minimum-bias (min-bias) trigger detector, which initiates the recording of an event. Here, min-bias refers to applying the minimum number of requirements to an event before acceptance. In Run 15, the requirement for a min-bias trigger is  $> 0$  PMTs above threshold. However in addition to providing the min-bias trigger for Run 15, the BBC was used to implement a high-multiplicity trigger in order to enhance the amount of the top 5% highest multiplicity events. The enhancement can be seen in Figure (TBA). This will be further discussed in Sec. (TBA). Also, the BBC was used to determine the event centrality by summing the charge collection of each BBC element; it is assumed the larger the charge collection the more central the event. This will be further discussed in Sec. (TBA) Moreover, the BBC can measure event plane using. For further BBC event plane calculation details see section (TBA).

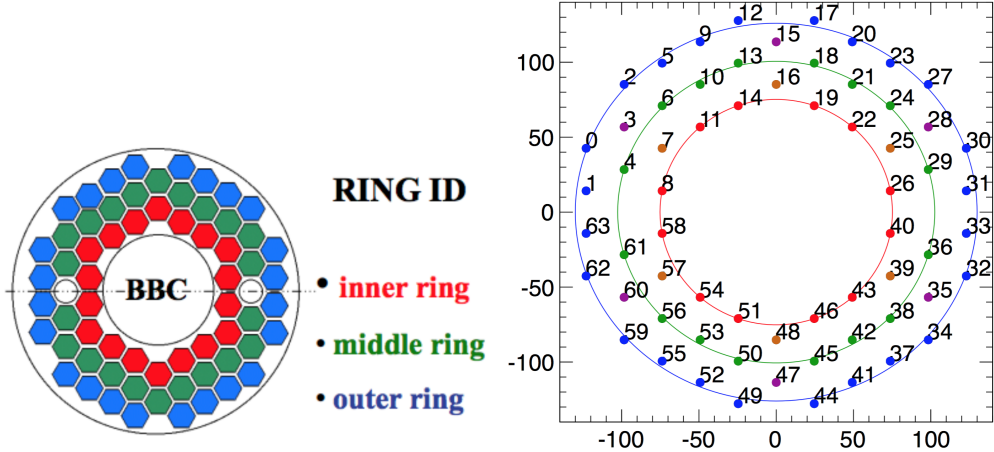


Figure 3.2: TBA

### 3.2.2 Forward Rapidity Detectors

#### 3.2.2.1 Forward Vertex Detector (FVTX)

The Forward Silicon Vertex Tracker (FVTX) consists of two identical endcaps covering a pseudorapidity range of  $1 < |\eta| < 3$  and an azimuth range of  $0 < \phi < 2\pi$ . Each one has four stations of silicon mini-strip sensors with a pitch of  $75 \mu m$  arranged in the radial direction around the beam pipe. The basic unit of construction is a wedge that has a silicon strip sensor and read-out chips. There are 4 FVTX layers in each endcap and they vary in radial extent.

#### 3.2.2.2 FVTX Clustering

#### 3.2.3 Midrapidity Detectors

##### 3.2.3.1 Drift Chamber

The Drift Chamber (DC) consists of two gas wire chambers, one located in each arm, and is used to measure particle trajectories in the  $r-\phi$  plane with the primary goals of measuring the particles transverse momentum ( $p_T$ ) and providing an anchoring point for the tracking. The DC is the innermost subsystem in the central arms, 2 m from the z-axis, placing them in a residual magnetic field of 0.6 kG. Each DC is cylindrical in design and covers 2 m along the beam direction

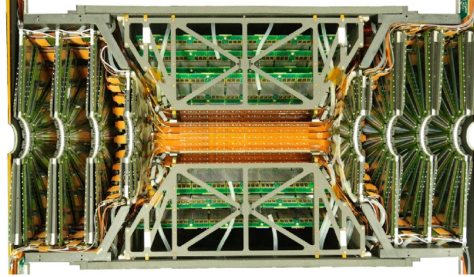


Figure 3.3: FVTX/VTX cut

and is 0.4 m thick, with the DC located in the West arm being a mirror image of that located in the East arm. A gas mixture of 50% Ar and 50% Ethane is used in each of the detectors. Each detector is divided into 20 equal sectors covering 4.5 degrees in  $\phi$ . Each sector contains six types of wire modules stacked radially and labeled X1, U1, V1, X2, U2, V2, respectively from the inside out. The X wires run parallel to the beam to perform precise 4  $\phi$  measurements while the U and V wires are set at small angles of about 6 degrees relative to the X wires to provide information about the z position of the track. A diagram of the wire layout in each sector is shown in Figure (TBA). In total, the DC consists of 6500 anode wires leading to 13,000 readout channels, with a measured single wire resolution of 165 m and a spatial resolution of 2mm.

### 3.2.3.2 Pad Chambers

The Pad Chambers (PC) are multiwire proportional chambers which consists of three separate layers of detectors measuring precise hit positions and making up the bulk of the PHENIX tracking system. The innermost layer, PC1, is located in both the East and West arms immediately outside the DC, providing a measurement of the z position at the back plane of the DC. The second layer, PC2, is located behind the RICH in the West arm only. The outer layer, PC3, is located just inside the EMCal in both arms and provides a second point on the straight line trajectories of the tracks through the detector, outside of the magnetic field.

### **3.2.3.3 Ring Imaging Cherenkov Detector**

The Ring Imaging Cherenkov (RICH) detector is located immediately behind the PC1 and provides the primary electron identification for PHENIX, in conjunction with the EM Cal. The RICH consists of two identical detectors located in each arm and provides e over pi discrimination below the pion Cherenkov threshold of 4.65 GeVc in the CO<sub>2</sub> gas used in the detectors.

### **3.2.3.4 EM Cal**

The Electromagnetic Calorimeter (EM Cal) is the outermost subsystem in the central arms and is designed primarily to measure the energies and positions of photons and electrons. It also plays a key role in the identification of as well as providing triggering for rare events. Two different EM Cal designs were utilized with 6 sectors based on a lead- scintillator design and 2 sectors based on a lead-glass design. The two different designs were chosen deliberately as each provides advantages and disadvantages, for instance the lead glass has a better energy resolution, while the lead scintillator has better linearity and timing.

### **3.2.3.5 Silicon Vertex Detector (SVX)**

## **3.2.4 DAQ**

Both the event rate and the event size are large at RHIC and therefore a system which can make decisions event by event and select events containing rare signals is necessary. The online data acquisition system (DAQ) and collects signals from the various subsystems and then processes the event acceptance decision based on various triggers.

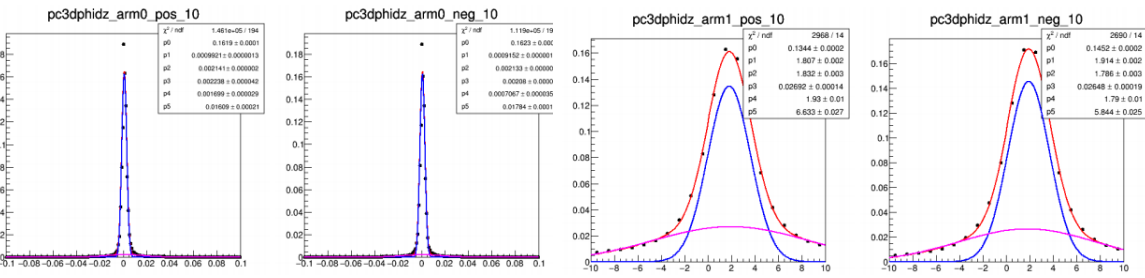


Figure 3.4: TBA

### 3.2.4.1 Triggering

## 3.3 Event Reconstruction and Characterization

### 3.3.1 Central Arm Tracking

### 3.3.2 CNT Tracks Simulation

### 3.3.3 Centrality Determination

### 3.3.4 Vertex Determination

## 3.4 Run15 pAu Dataset

### 3.4.1 Beam Geometry Effects

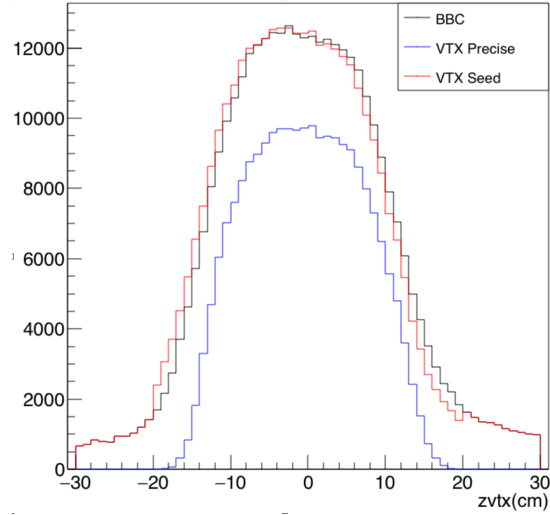


Figure 3.5: TBA

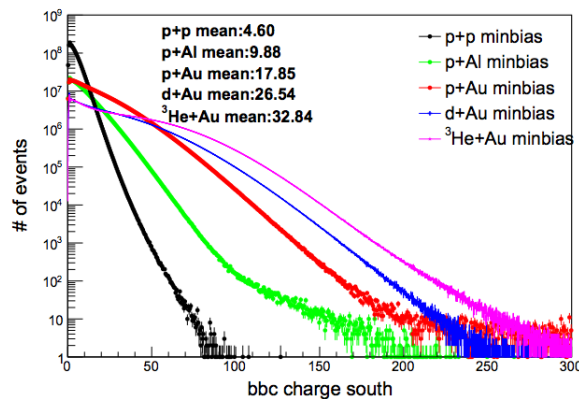


Figure 3.6: TBA

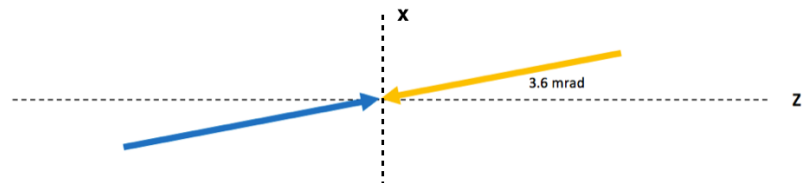


Figure 3.7: A vector diagram illustrating the yellow and blue beam angle.

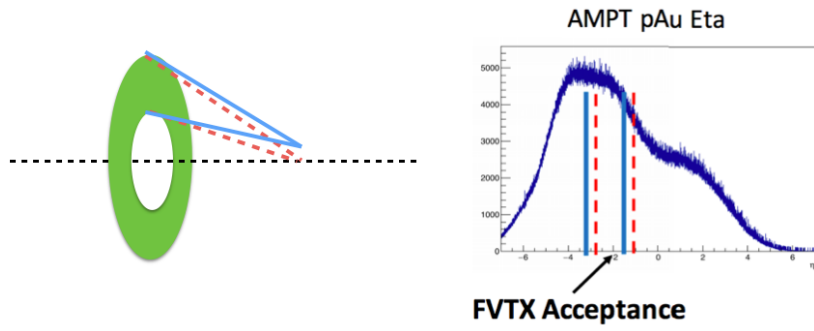


Figure 3.8: On the left is a cartoon diagram illustrating  $\eta$  acceptance shift due to a beam offset in one of the FVTXs layers. The right plot shows the AMPT distribution of particles for pAu @ 200 GeV and the shifted  $\eta$  acceptance.

## Chapter 4

### Analysis

#### 4.1 Direct Observables: Building Blocks of the Measurement

**TO DO: ADD A FIGURE OF THE PHENIX COORDINATE SYSTEM**

##### 4.1.1 Central Arm Tracks

This analysis use central arm tracks. A central arm track is a charged particle emitted from the heavy ion collision and detected by the PHENIX central arms. There are 2 central arms and each one covers  $\eta < |0.35|$  and  $\frac{\pi}{2}$  in azimuth. The drift chamber provides momentum information and the pad chambers provide track quality metrics. The RICH provides electron identification. The physics parameters of central arm tracks relevant to this analysis is the momentum vector:  $p = (p_x, p_y, p_z)$ . The momentum of CNT tracks is defined at the collision vertex. CNT have good momentum resolution (**TO DO: QUANTIFY THIS**). In p+Au collisions, the average number of reconstructed CNT (before cuts) is (**TO DO: QUANTIFY THIS**).

##### 4.1.2 FVTX Clusters

This analysis uses clusters from the forward vertex detector (FVTX). The FVTX detects charged particles traveling through its silicon layers. The intersection between the charged particle and the FVTX detector is recorded in each of the 4 layers the particle goes through. Each intersection is known as a cluster. Each cluster is thought to be produced from a single charged particle. These clusters have a position resolution in x and y ( or r and  $\phi$ ) (**TO DO: QUANTIFY THIS**)

and have a z resolution that is the width of the FVTX layer. The FVTX acceptance is  $1 < |\eta| < 3$  and spans the full azimuth.

#### 4.1.3 BBC PMTs

This analysis uses photomultipliers (PMTS) from the beam beam counter (BBC). The BBC detects charged particles traveling through its scintillator material. The BBC acceptance is  $3.1 < |\eta| < 3.9$  and spans the full azimuth. The BBC provides position information in x, y, and z and, like the FVTX, the x and y (or r and  $\phi$ ) resolution differ from the z resolution in that the z resolution is simply the width of the active area of the BBC. In addition to position information, the BBC provides charge information which is calibrated to roughly correspond to the number of charged particles detected by each PMT per event.

### 4.2 Event Plane Method

The event plane method is a way of measuring the long range correlations in the spray of particles from a heavy ion collision. The event plane method works by calculating a mathematical object from the data called an event plane. This event plane is defined for each flow harmonic and is sometimes denoted as  $\Psi_n$ . The definition for  $\Psi_n$  is related to the calculation of the Q-vector:

$$Q_x = \sum (w_i * \cos(n * \phi_i)) \quad (4.1)$$

$$Q_y = \sum (w_i * \sin(n * \phi_i)) \quad (4.2)$$

$$Q_w = \sum (w_i) \quad (4.3)$$

$$\Psi_n = \arctan\left(\frac{Q_y}{Q_x}\right). \quad (4.4)$$

The  $Q_w$  component of the Q-vector is only used during the event plane calibration. Once the event plane has been calculated, the flow harmonics ( $v_n$ ) are calculated as

$$v_n = \frac{\langle\langle \cos(n(\phi - \Psi_n)) \rangle\rangle}{Resolution(\Psi_n)}, \quad (4.5)$$

where  $\langle\langle \rangle\rangle$  means averaged over each event and each  $\phi$  value and the resolution of  $\Psi_n$  is calculated using the 3-subevent method. It is important to note the the set of particles used to calculate  $\Psi_n$

and  $\phi$  must be different in order to avoid autocorrelations. This is usually done by imposing an  $\eta$  gap between two particle sets.

For this analysis, the event plane is calculated separately for each of the forward detectors mentioned above, the BBC and the FVTX. For the FVTX, the Q-vector is calculated in each event as

$$Q_x = \sum_i^{NFVTXClus} (\cos(n * \phi_i)) \quad (4.6)$$

$$Q_y = \sum_i^{NFVTXClus} (\sin(n * \phi_i)) \quad (4.7)$$

$$\phi_i = \arctan\left(\frac{FVTXClus_y^i}{FVTXClus_x^i}\right) \quad (4.8)$$

where  $NFVTXClus$  is the number FVTX clusters in that event and  $FVTXClus_{y,x}^i$  are the  $x$  and  $y$  components of the  $i$ th FVTX Cluster in that event. This Q-vector is calculated with no cluster dependent weight factor as each cluster is taken to be equal weight (since no charge information is available in the FVTX).

For the BBC, the Q-vector is calculated in each event as

$$Q_x = \sum_i^{NPMT} (w_i \cos(n * \phi_i)) \quad (4.9)$$

$$Q_y = \sum_i^{NPMT} (w_i \sin(n * \phi_i)) \quad (4.10)$$

$$Q_w = \sum_i (w_i) \quad (4.11)$$

$$\phi_i = \arctan\left(\frac{PMT_y^i}{PMT_x^i}\right) \quad (4.12)$$

where  $w_i$  is the charge collected on the PMT and  $NPMT$  is the number of PMTs that fired (above threshold) in each event.

Finally, the  $v_n$  are calculated using a combination of the BBC or FVTX Q-vectors and the CNT tracks as

$$v_n = \frac{\left\langle \left\langle \cos(n(\phi^{CNT} - \Psi_n^{BBC,FVTX})) \right\rangle \right\rangle}{Resolution(\Psi_n^{BBC,FVTX})}. \quad (4.13)$$

In this analysis, I will be exclusively focusing on the second harmonic  $v_2$ . The reason for this is two-fold:

- (1) The second harmonic is usually the largest and easiest to measure harmonic.
- (2) The second harmonic is physically interesting because it is thought to correspond with flow.

The first harmonic is thought to correspond momentum conservation.

#### 4.2.1 Event Plane Flattening Calibration

In order for the event plane to be a useful in making a  $v_n$  measurement, the event plane must be calibrated. For the event plane method, a physical assumption is made that the true distribution of  $\Psi_n$  angles will be uniform. In other words, there is no preferred event plane angle in heavy ion collisions; on average there should be an equivalent amount of events where the event plane is oriented at 0 radians and at  $\frac{\pi}{2}$ . So if the measured  $\Psi_n$  distribution is not flat then it could come from a variety of sources such as variations in the efficiency of detecting charged particles as a function of  $\phi$ . Thus, the event plane calibration seeks to restore the  $\Psi_n$  distribution to the physical expectation of uniformity.

The method used in this analysis to achieve this is a "re-centering" and "flattening" calibration. In order to better understand this calibration, it is useful to examine an example uncalibrated  $\Psi_n$  distribution. The red curve in Fig. 4.2.1 depicts a significant deviation from uniformity in the  $\Psi_2$  distribution which would distort the  $v_2$  measurement. A combination of effects cause there to be a depletion of  $\Psi_2$  values at 0.0 radians and an enhancement at  $\frac{\pi}{2}$  radians. The flattening calibration attempts to offset this lack of uniformity by systematically shifting each event's raw  $\Psi_2$  value by an amount corresponding to the amount the  $\Psi_2$  distribution is nonuniform. The more that the raw  $\Psi_2$  distribution is nonuniform, the more significant that the flattening calibration must systematically shift each  $\Psi_2$  value in order to restore uniformity. Thus, it is in the analyzer's best interest to provide the flattest possible  $\Psi_2$  distribution before performing the flattening calibration.

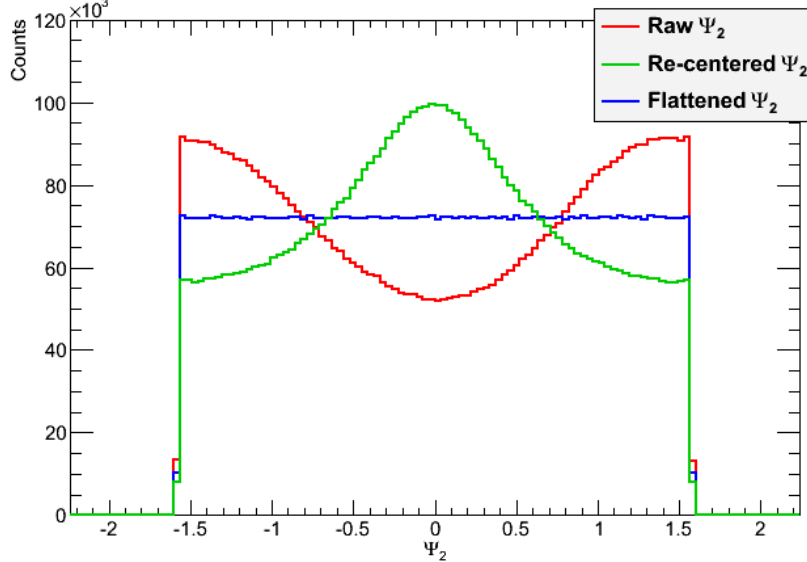


Figure 4.1: This is the FVTX-S  $\Psi_2$  distribution projected over all z-vertex bins at different steps during the calibration. The range of the  $\Psi_2$  resolution is from  $-\frac{\pi}{2}$  to  $\frac{\pi}{2}$  because of the periodicity. The raw (in red)  $\Psi_2$  distribution has a sinusoidal shape. The re-centered (in green)  $\Psi_2$  distribution moves the peak to 0.0 radians and changes the width. The flattened (in blue)  $\Psi_2$  distribution spread out the counts so that there is uniformity. Each calibration step preserves the integral.

The flattening calibration requires two steps to completely flatten the  $\Psi_n$  distribution. The first step of the calibration is to re-center the peak of the raw  $\Psi_n$  distribution to be at 0.0 radians and to resize the width of the peak. The second step is to Fourier transform the re-centered distribution and use the transformation to shift the  $\Psi_n$  values to a uniform distribution. With flattening, each  $\Psi_n$  is transformed to  $\Psi_n + \Delta\Psi_n$  where  $\Delta\Psi_n$  is defined as

$$\Delta\Psi_n = \sum_{i=1}^N \left( \frac{2}{i} (\sin(i\Psi) F_i^{\cos}(f(\Psi_n)) - \cos(i\Psi) F_i^{\sin}(f(\Psi_n))) \right), \quad (4.14)$$

where  $N$  is the number of components,  $F_i^{\cos}(f(x))$  is the  $i$ th component of the cosine Fourier transform of  $f(x)$ , and  $f(\Psi_n)$  is the  $\Psi_n$  distribution.

For this analysis,  $N = 12$  is a sufficient number of components to flatten the  $\Psi_n$  distribution. The re-centering and flattening calibration is done 30 z-vertex bins.

#### 4.2.2 Event Plane Resolution Calculation

As mentioned above, the event plane resolution calculation is done using the standard 3-sub event method. The strategy of this method is to leverage the measurement of  $\Psi_n$  in different detectors for the same event in order to constrain how well each detector measures  $\Psi_n$ . The definition of the event plane resolution is

$$Res(\Psi_n^A) = \sqrt{\frac{\langle\cos(n(\Psi_n^A - \Psi_n^B))\rangle \langle\cos(n(\Psi_n^A - \Psi_n^C))\rangle}{\langle\cos(n(\Psi_n^B - \Psi_n^C))\rangle}}, \quad (4.15)$$

where A,B, and C are three detectors measuring the same event, or each detector measuring a "sub event".

In this analysis, the three detectors that are available are FVTX-S, the BBC-S, and the CNT which have  $\eta$  ranges of  $-3 < \eta < -1$ ,  $-3.9 < \eta < 3.1$ , and  $|\eta| < 0.35$  respectively. However, due to the fact that the CNT detector does not have full azimuthal coverage, the CNT event plane is not well defined for a class of events where the event plane doesn't point into the CNT acceptance, therefore the event plane resolution is calculated via a modified yet mathematically equivalent definition to the one mentioned above. This modified method allows the resolution of the FVTX-S and the BBC-S to be calculated using the CNT without having to calculate CNT event plane. It is defined as

$$Res(\Psi_n^A) = \sqrt{\frac{\langle\langle\cos(n(\Psi_n^A - \phi^{CNT}))\rangle\rangle \langle\cos(n(\Psi_n^A - \Psi_n^C))\rangle}{\langle\langle\cos(n(\phi^{CNT} - \Psi_n^C))\rangle\rangle}}, \quad (4.16)$$

where there is a double average over each CNT track and each event. (**TO DO: Make a Table of Default Event Plane Resolutions**)

#### 4.3 good run list

#### 4.4 luminosity over time

#### 4.5 bbc charge

#### 4.6 central events

look at jamie's central AN pau

The idea of the event plane flattening and recentering calibration is to obtain an uniform distribution of  $\Psi_n$  which is the physical expectation.

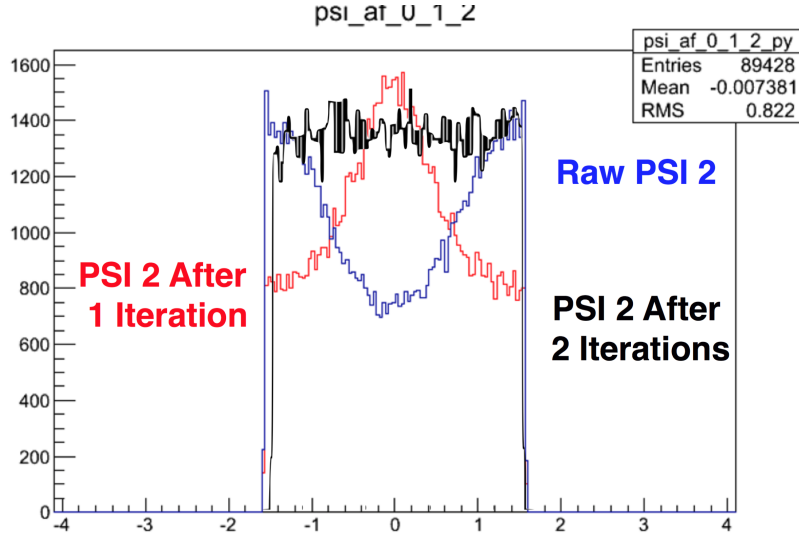


Figure 4.2: TBA

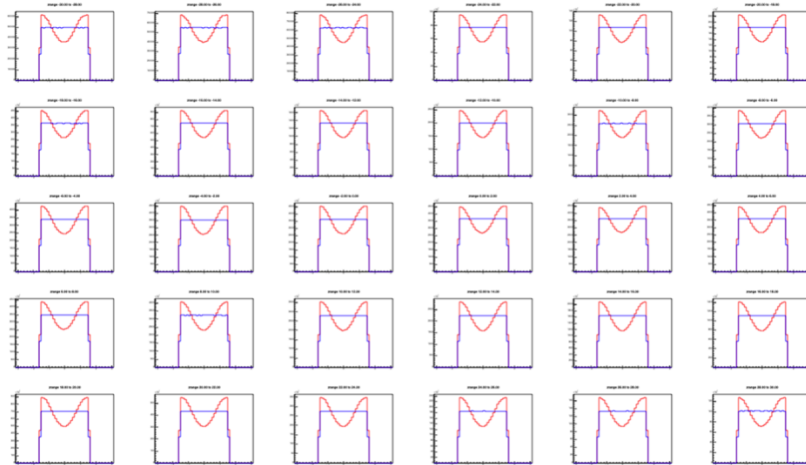


Figure 4.3: BBC Psi2 EP distribution in different  $z$  vertex bins red before flattening, blue after flattening.

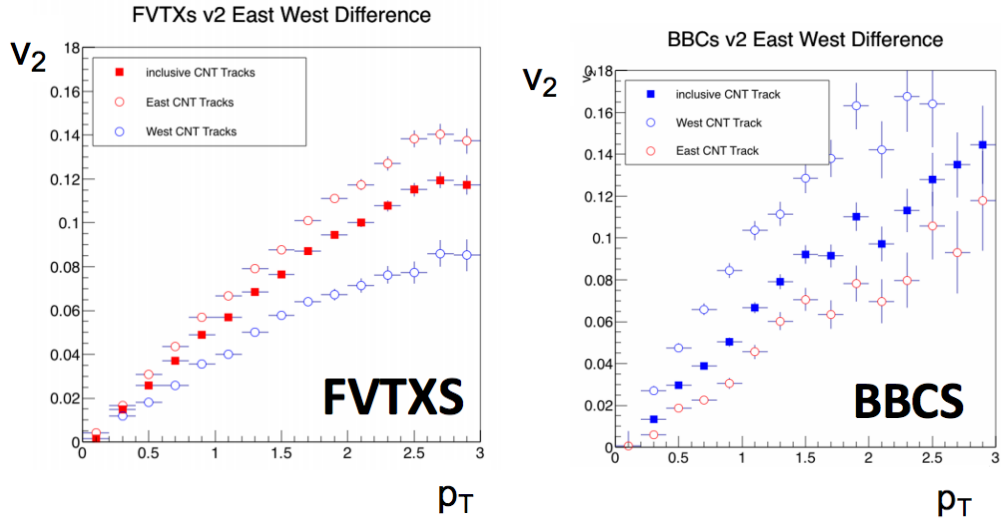


Figure 4.4: The left plot shows the FVTX EP East West Difference without any corrections and the right plot shows the BBC EP East West Difference without any corrections.

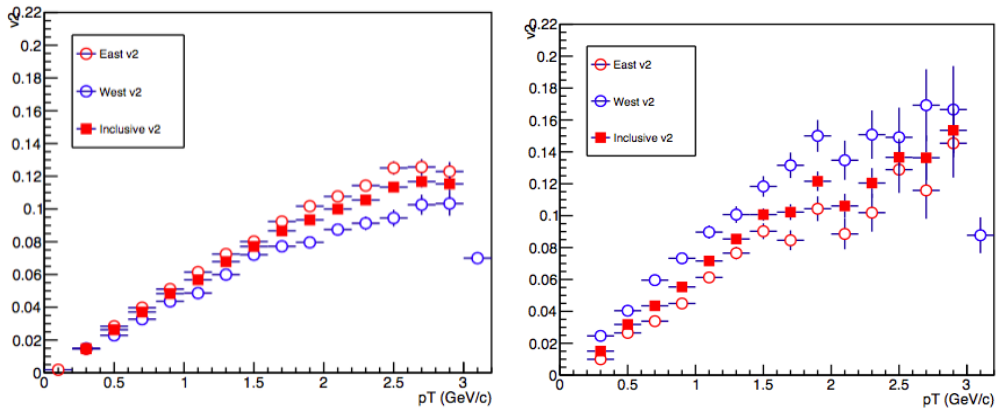


Figure 4.5: The left plot shows the FVTX EP East West Difference with beam rotation and vertex offset corrections and the right plot shows the BBC EP East West Difference with the same corrections.

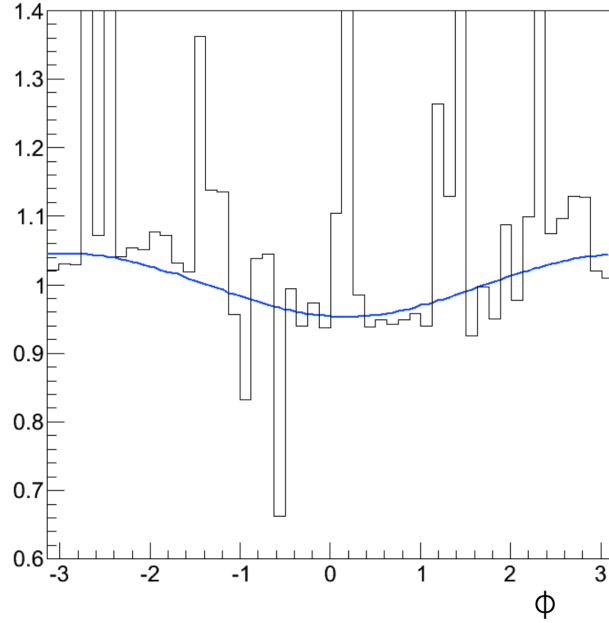


Figure 4.6: TBA

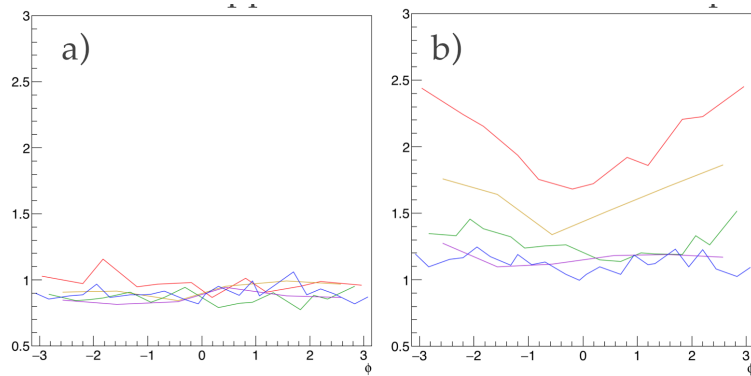


Figure 4.7: These figures show the phi distribution of BBC PMT charge in a) the Run15 pp dataset and in b) the Run15 pAu dataset.

#### 4.6.1 Correcting for Beam Geometry

#### 4.7 Systematic Error Estimate

##### 4.7.1 Non-flow Estimate

##### 4.7.2 Pile Up

##### 4.7.3 Beam Angle

##### 4.7.4 Track Background

##### 4.7.5 Event Plane Detectors Agreement

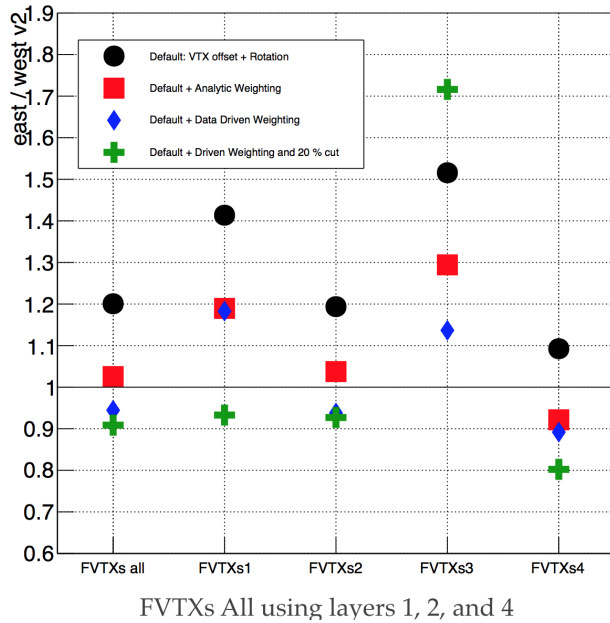
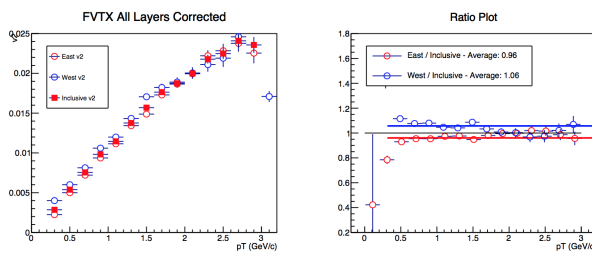


Figure 4.8: TBA

Figure 4.9: FVTX EP corrected with inverse  $\phi$  weighting and 20 % cut.

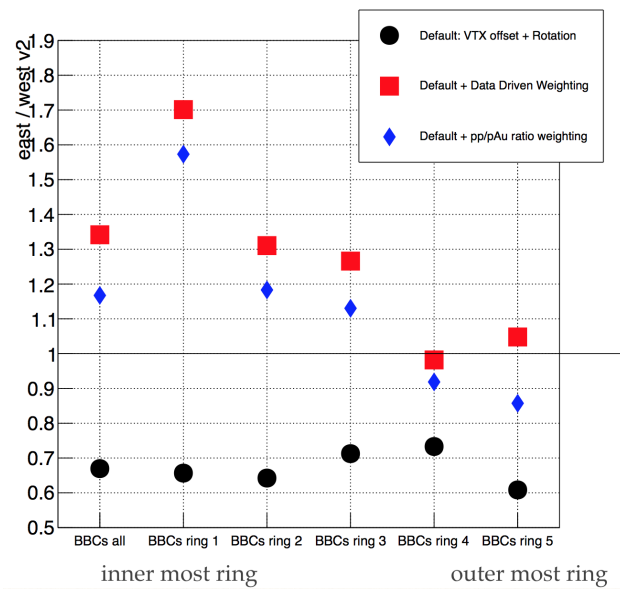


Figure 4.10: TBA

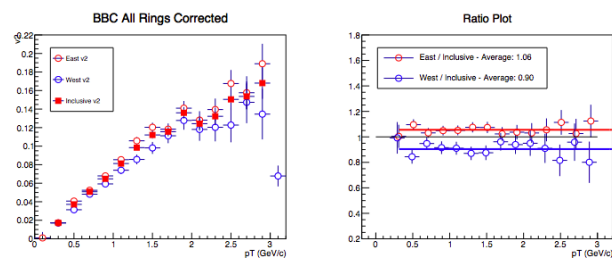


Figure 4.11: BBC EP corrected with pp, pau ratio weighting.

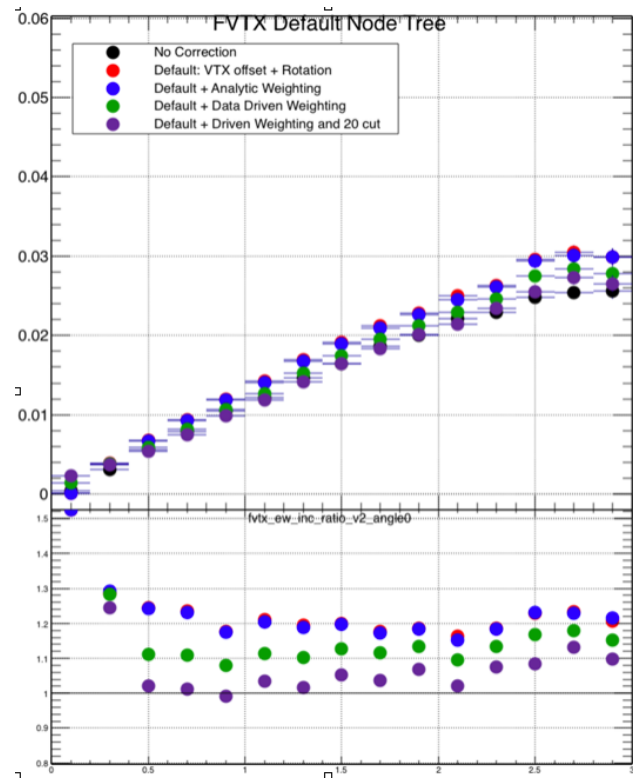


Figure 4.12: A comparison of FVTX EP  $v_2$  corrections on the inclusive measurement.

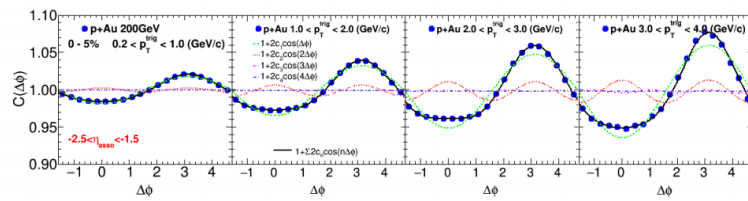


Figure 4.13: TBA

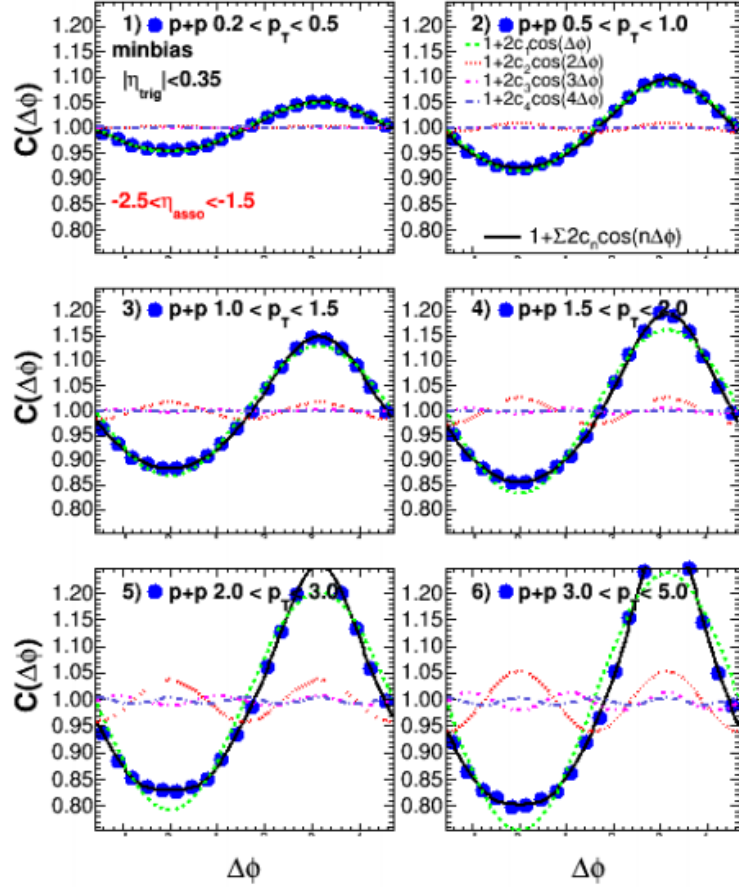


Figure 4.14: TBA

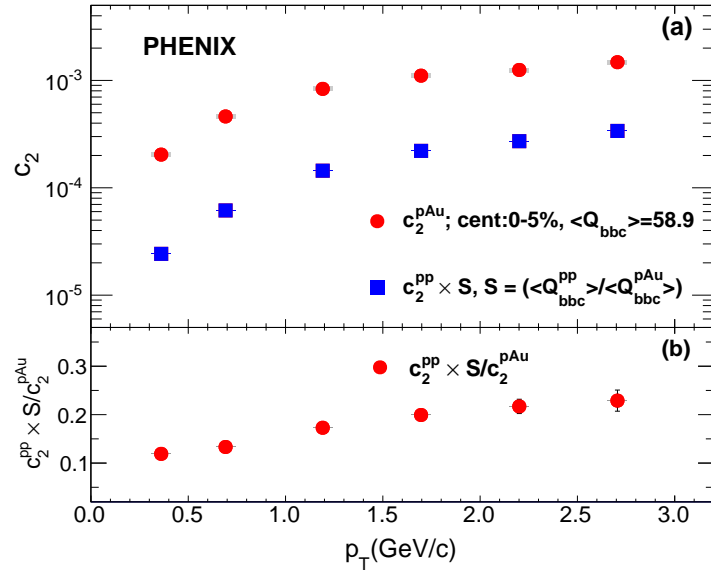


Figure 4.15: TBA

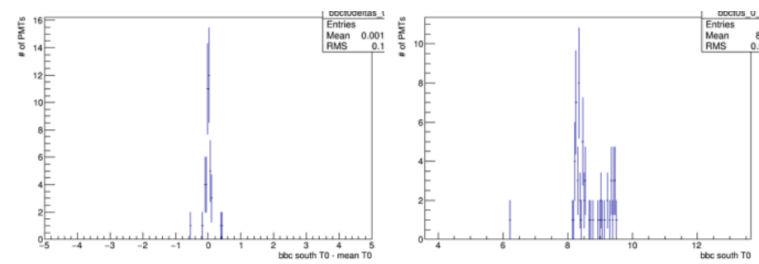


Figure 4.16: The left plot is an example of a normal event, the right plot is an example pile up event.

## **Chapter 5**

### **Discussion of Results**

#### **5.1 $v_2$ Measurement**

##### **5.1.1 $v_2$ vs $p_T$**

##### **5.1.2 $v_2$ vs Multiplicity**

#### **5.2 Comparison with Theory**

##### **5.2.1 SONIC**

##### **5.2.2 AMPT**

##### **5.2.3 IP-Glasma with Hydro**

#### **5.3 Comparison with Other Species**

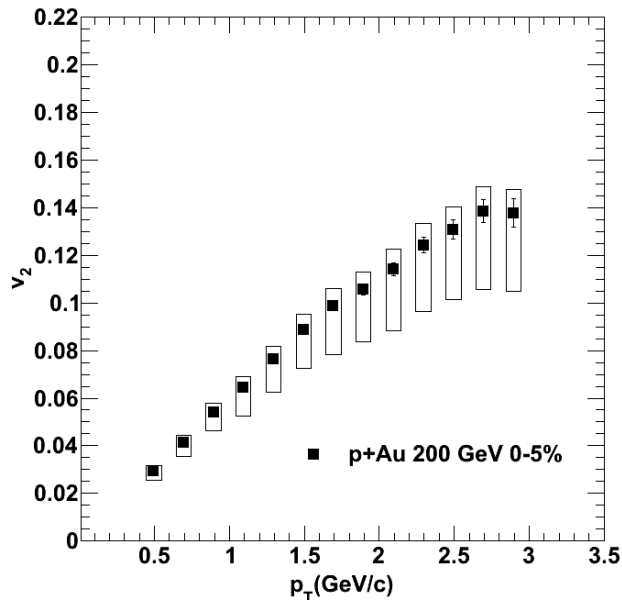


Figure 5.1: TBA

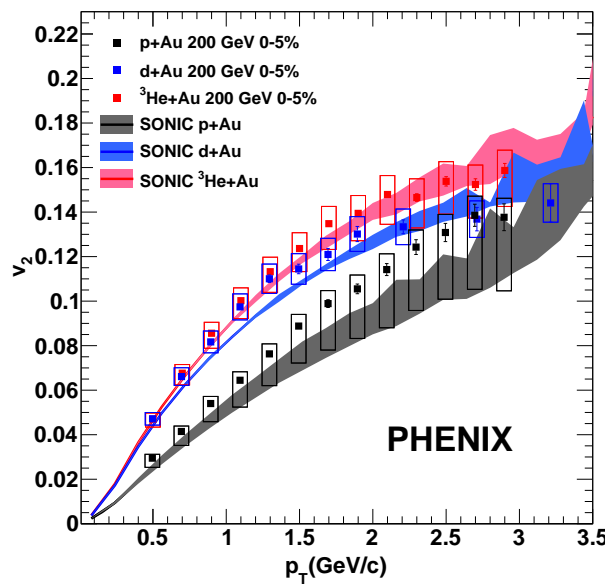


Figure 5.2: TBA

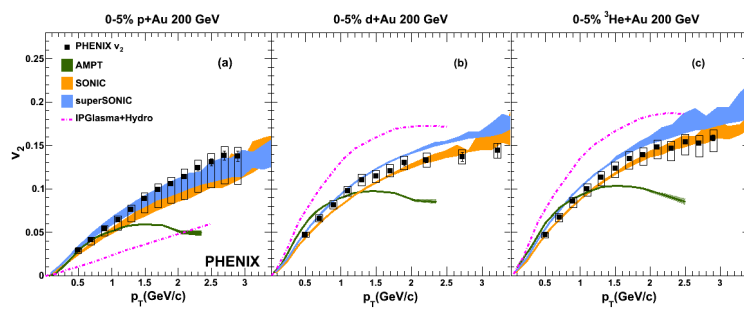


Figure 5.3: TBA

## **Chapter 6**

### **Summary and Outlook**